Geophysical Research Letters

RESEARCH LETTER
10.1029/2019GL082842

Tidal and Thermal Stresses Drive Seismicity Along a Major Ross Ice Shelf Rift

S. D. Olinger[1,2], B. P. Lipovsky[2], D. A. Wiens[1], R. C. Aster[3], P. D. Bromirski[4], Z. Chen[4], P. Gerstoft[4], A. A. Nyblade[5], and R. A. Stephen[6]

[1]Department of Earth and Planetary Sciences, Washington University in St. Louis, St. Louis, MO, USA, [2]Department of Earth and Planetary Sciences, Harvard University, Cambridge, MA, USA, [3]Department of Geosciences, Colorado State University, Fort Collins, CO, USA, [4]Scripps Institution of Oceanography, University of California, San Diego, La Jolla, CA, USA, [5]Department of Geosciences, Penn State University, University Park, PA, USA, [6]Woods Hole Oceanographic Institution, Woods Hole, MA, USA

Key Points:
- 2,515 icequakes associated with rift deformation on the Ross Ice Shelf are located using a double-difference location algorithm
- Icequake timing correlates with tidal phase diurnally and inversely correlates with air temperature on multiday and seasonal time scales
- Ocean swell, infragravity waves, and a significant tsunami arrival are not correlated with increased rift activity

Supporting Information:
- Supporting Information S1
- Figure S1
- Figure S2
- Figure S3

Correspondence to:
S. D. Olinger,
setholinger@fas.harvard.edu

Citation:
Olinger, S., Lipovsky, B. P., Wiens, D., Aster, R. C., Bromirski, P. D., Chen, Z., et al. (2019). Tidal and thermal stresses drive seismicity along a major Ross Ice Shelf rift. *Geophysical Research Letters*, *46*, 6644–6652. https://doi.org/10.1029/2019GL082842

Received 15 MAR 2019
Accepted 16 MAY 2019
Accepted article online 23 MAY 2019
Published online 20 JUN 2019

Abstract Understanding deformation in ice shelves is necessary to evaluate the response of ice shelves to thinning. We study microseismicity associated with ice shelf deformation using nine broadband seismographs deployed near a rift on the Ross Ice Shelf. From December 2014 to November 2016, we detect 5,948 icequakes generated by rift deformation. Locations were determined for 2,515 events using a least squares grid-search and double-difference algorithms. Ocean swell, infragravity waves, and a significant tsunami arrival do not affect seismicity. Instead, seismicity correlates with tidal phase on diurnal time scales and inversely correlates with air temperature on multiday and seasonal time scales. Spatial variability in tidal elevation tilts the ice shelf, and seismicity is concentrated while the shelf slopes downward toward the ice front. During especially cold periods, thermal stress and embrittlement enhance fracture along the rift. We propose that thermal stress and tidally driven gravitational stress produce rift seismicity with peak activity in the winter.

Plain Language Summary In Antarctica, large bodies of floating ice called ice shelves help prevent ice on land from sliding into the ocean. To predict how Antarctica might respond to climate change, we need to understand how ice shelves interact with the environment, including the atmosphere and the ocean. The largest ice shelf, the Ross Ice Shelf, is over 500,000 km^2 in area, making it the largest body of floating ice in the world. In this study, we deployed nine seismographs, the same instruments used to study earthquakes, to monitor vibrations and cracking within the Ross Ice Shelf over a 2-year period. During that time, the instruments detected nearly 6,000 fracture events along a 120-km-long crack in the ice shelf. We compared the timing of the cracking to air temperature data, ocean wave activity, and tides to see whether these factors influenced the crack's behavior. We found that fracture occurs most frequently just after high tide during winter and when the air is very cold. We also found that fracture at the rift is not triggered by ocean waves. This work demonstrates that Antarctic ice shelves are very sensitive to the environment and highlights the need to continue studying them.

1. Introduction

The need to understand marine ice sheet stability under various climate scenarios has fueled ongoing discourse about the nature and forcing of fracturing processes in floating ice shelves. Brittle deformation of large ice shelves is dominated by the propagation of large, through-cutting fracture-propagated rifts (Benn et al., 2007). Debate has largely focused on the relative importance and interactions of ocean wave-induced stresses (Banwell, 2017; Bromirski & Stephen, 2012; Bromirski et al., 2010, 2015; Brunt et al., 2011; Cathles et al., 2009; Holdsworth & Glynn, 1978; MacAyeal et al., 2008; Massom et al., 2018), glacial stresses (Bassis et al., 2005; Hulbe et al., 2010a; LeDoux et al., 2017), and rift-filling melange (Fricker et al., 2005; Larour et al., 2004; MacAyeal et al., 1998; Rignot & MacAyeal, 1998). Seismic observations have the ability to quantify small-scale brittle deformation in the form of icequakes and thus provide an efficient means to investigate the spatial and temporal extent of ice shelf fracture processes (Bassis et al., 2007; Heeszel et al., 2014; Hulbe et al., 2016; Lipovsky, 2018).

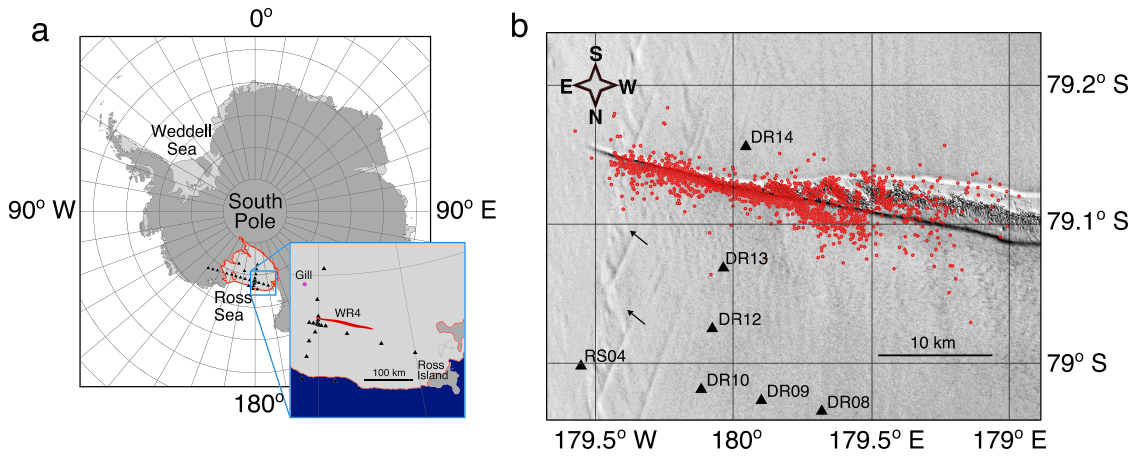

Figure 1. Study site and icequake locations. (a) Locations of rift WR4, the seismograph array, and weather station Gill on the Ross Ice Shelf. Data from stations DR07 and DR06 (not shown) were additionally used to locate icequakes. (b) Locations of 2,515 icequakes at WR4. East of about 180°, icequake locations fall along central axis of rift; west of 180°, icequake locations fall along en echelon features within the rift-filling melange. Arrows indicate suture zone fabric.

As part of two coupled projects to study the dynamics of the Ross Ice Shelf (RIS) and the solid Earth structure beneath (Bromirski et al., 2015), nine broadband seismographs were deployed spanning both sides of a large rift located about 150-km south of the RIS front (Figure 1), denoted as WR4 (Walker et al., 2013). This deployment provides an important opportunity to investigate the role of various processes that drive ice shelf fracture. LeDoux et al. (2017) found that rift WR4's eastern tip is currently located adjacent to a suture zone, a region of deformed ice that arrests rift propagation, and multiyear imagery has confirmed that WR4 is not actively propagating (Walker et al., 2013). Despite WR4's apparent inactivity, the RIS array detected numerous icequakes in the vicinity of the rift, which we use to determine whether the rift is undergoing active brittle deformation and to provide constraints on the forces influencing rift propagation.

2. Data

2.1. Seismic Data

This study uses data collected by two simultaneous collaborative seismograph deployments on the RIS. We use nine seismic stations deployed along two lines that intersect near 78.96°S, 179.88°W (Figure 1). These stations are a subset of the 34 seismic stations that were deployed across a much larger region (Figure 1). Each station consisted of a Nanometrics T120 PHQ broadband seismometer buried about 1 m into the firn recording at 200 samples per second and a Quanterra Q330 datalogger. The equipment was powered by solar panels in the austral summer and by lithium batteries in the winter. The instruments were deployed in November 2014, and the first year of data was retrieved November–December of 2015. The instruments were recovered, and the final year of data was retrieved in November–December of 2016.

2.2. Weather and Environmental Data

Temperature data from the Automatic Weather Station project were used to investigate whether seismicity is correlated with meteorological phenomena. The Automatic Weather Stations are deployed across Antarctica and record temperature, pressure, wind speed, and humidity (Lazzara et al., 2012). Because of its proximity to the array and the completeness of its records, we use data from station Gill, located at 79.823°S, 178.536°W at a distance of 80 km from the center of the array.

3. Methods

3.1. Detection and Location

We utilized an automated short-term average/long-term average event detection routine to form a catalog of any local activity recorded on stations with a high signal-to-noise ratio. We detected 5,948 unique events throughout both years of data after manually removing all detections of nonlocal seismicity. To generate arrival times and to analyze the similarity of the detected events, we applied a cross correlation and clustering algorithm to the entire data set. However, the events did not exhibit high correlation values, and the clusters generated were not consistent across different stations and components, indicating that, unlike

many icequakes, the events are not true repeating events. A typical event waveform is shown in supporting information Figure S1.

We initially located a subset of the largest events from 2015 using manually picked *P* and *S* wave arrival times. However, direct *P* and *S* wave arrivals were often small and emergent, making it difficult to pick arrival times consistently. Because vertical component Rayleigh wave arrivals were much easier to identify, we located the entire data set using Rayleigh wave arrival times. We calculated envelope functions for each event waveform on DR14, DR13, DR12, DR11, DR10, DR09, DR08, DR07, and RS04. Because these icequake waveforms are dominated by surface waves, the maximum value of each envelope function corresponds to the arrival of Rayleigh waves. A short-term average/long-term average threshold was also applied to prevent incorrect identification of arrivals. Using this process, Rayleigh arrival times were automatically generated for all 5,948 events.

We located the events that had Rayleigh phase arrivals on more than five stations. We first used a simple grid-search algorithm that minimized the misfit between observed and predicted Rayleigh arrivals by calculating a summed squared error for each potential location in the grid and selecting the lowest error point. In order to calculate misfit, we back-propagated the arrivals and took the mean time as the origin time. Once satisfactory locations were obtained from the grid search, we removed arrivals from stations with travel time residuals greater than 1 s for each event. Events now with less than five arrivals were removed, and the remaining events were relocated using a standard iterative least-squares inversion. From the resulting locations, those with location and origin time standard deviations greater than 2 km and 2 s were removed, and the remaining 2,515 events were relocated using a double-difference relative location method.

To determine an accurate Rayleigh phase velocity for use in event relocation, grid-search locations were calculated using an initial velocity of 1.5 km/s. We then selected all events aligned with DR13, DR12, and DR10 and calculated the time difference between arrivals on DR13 and DR12, DR13 and DR10, and DR12 and DR10 to obtain estimates of Rayleigh velocity largely independent of source locations. A least-squares inversion was then used to determine the velocity that minimized the misfit between the observed and predicted arrival time differences calculated using the known distances between stations. This calculation resulted in a Rayleigh velocity of 1.55 km/s, which was then used in the grid-search, linearized inversion, and double-difference location methods. This Rayleigh wave velocity is similar to that predicted for a structure of slow velocity firn overlying ice.

3.2. Comparison With Environmental and Weather Phenomena

To investigate the relationship between rift seismicity and the atmosphere, we compare the timing of seismicity with Automatic Weather Station air temperature data from 2015 and 2016 (Lazzara et al., 2012). We also compare the timing of events with tidal phase and tidal slope. Tidal heights were obtained by running the CATS2008 model, an update to the model described by Padman et al. (2002), for the duration of the deployment at the center of the array (DR10). To find the time of each high tide, local maxima were calculated for the data set. We then calculated the difference in time between each event and the most recent high tide. The resulting times were binned by hour, yielding the number of events that occur in each hour after high tide. Finally, we divided by the total length of the corresponding tidal cycle to yield a measure of event timing binned by tidal phase. We calculated the slope at the ice shelf by running the CATS2008 model at both the grounding line (82°S, 164°E) and the front (78.5°S, 179°E), finding their difference, and dividing by the distance between the two points.

To investigate swell and infragravity (IG) waves, we made a spectrogram of the long-period horizontal north-south component data from DR10. Previous work by Bromirski et al. (2017) found that IG waves generate greater horizontal displacements than vertical displacements on RIS, so we used the horizontal component data for our analysis of ocean swell and IG waves. Before generating a spectrogram, we first removed the instrument response to displacement on the frequency band 0.015–0.2 Hz. To find swell band power, we integrated the spectrogram over the frequency band 0.03–0.15 Hz for each window used to produce the spectrogram. To find IG band power, we integrated the spectrogram over the frequency band 0.015–0.03 Hz for each window used to produce the spectrogram. These frequency limits were selected based on the ocean wave classification presented in Toffoli and Bitner-Gregersen (2017).

4. Characteristics and Locations of Rift Seismicity

Icequakes with high signal-to-noise exhibit distinct *P*, *S*, surface wave, and longitudinal plate wave arrivals (Press & Ewing, 1951). Icequake events are lower frequency than similarly sized tectonic earthquakes (Aki, 1967) with peak amplitudes between 1 and 4 Hz. In all cases, the icequake-associated surface waves have the largest amplitudes. We find that the icequakes range in size from $M_L = -2.5$ to $M_L = 0$ (supporting information S2), and there is evidence for a *b* value greater than 1 based on the statistics of larger magnitude events, indicating that this sequence of icequakes has a higher ratio of small to large events than predicted by a standard Gutenberg-Richter distribution. Typical waveforms are shown in Figure S1.

The icequake epicenters were located using a double-difference method and automated picks of peak Rayleigh wave arrival times on the vertical component seismogram. The icequakes are located along a 30-km segment of the rift (Figure 1), associated with three broad regional patterns of icequake activity. First, icequakes located east of about 180°E are aligned with the central axis of the rift. Because the observed icequakes have high amplitude surface waves relative to body waves, it is likely that the icequakes occur near the ice shelf surface (Lough et al., 2015). Possible sources include fracture along the upper edges of the rift walls and collision, settling, or fracture of the blocks of ice within the melange.

Second, many of the icequakes west of about 180°E occur along a series of en echelon features within the wider region of rift-filling melange. Because the standard deviations of relative icequake locations are typically around 100 m and because of the strong spatial association of the events with the en echelon shear zone features, we are confident that these events originated within the melange and were not incorrectly located events occurring along the rift walls. We therefore interpret this second group of icequakes to be caused by deformation of the rift-filling melange. Because events in the melange begin to occur where the rift widens, we speculate that the type of brittle ice shelf deformation recorded here may cause widening at the middle of the rift. See supporting information Figure S2 for a more detailed view of rift morphology.

Third, events decrease in number west of about 179.5°E, and distant events are typically less precisely located. To determine whether the apparent concentration of icequakes is an artifact of our network geometry, we examined the magnitude of the events at various positions along the rift. We find that the prevalence of low magnitude events decreases with distance from the intersection of the array and the rift, suggesting that the apparent decrease in seismicity away from the network may be the result of attenuation of similar-sized signals from more distant icequakes. It is therefore possible that relatively uniform levels of seismicity occur along the entire rift.

Icequakes are not clustered in front of the rift tip as was previously observed at the actively propagating Loose Tooth Rift in the Amery Ice Shelf (Bassis et al., 2008; Heeszel et al., 2014) but instead cease abruptly where the rift reaches the adjacent suture zone at around 179.5°W. This decrease in seismicity is not due to reduced array detection capability to the west, as very small events are detected in the rift near the rift tip. We interpret the lack of icequakes at the rift tip to indicate a lack of brittle deformation in this region. Since westward propagation of the WR4 rift tip has currently stagnated (LeDoux et al., 2017; Walker et al., 2013), our inferred lack of brittle deformation is therefore consistent with rift stagnation in suture zones (Borstad et al. (2017), Hulbe et al. (2010a), Kulessa et al. (2014), and McGrath et al. (2014)).

5. Ice Shelf Slope From Ocean Tides Controls Diurnal Patterns in Seismicity

We observe tidal modulation of the icequake activity (Figure 2a). As tides rise, the level of seismicity increases until about 5 hours after high tide, when the level of seismicity begins to fall. The timing of events within a day is well-correlated with the tidally modulated slope of the ice shelf, with the highest seismicity rates when the entire RIS slopes downward toward the ocean (Figure 2b). When the shelf tilts, a horizontal component of gravitational force arises in the plane of the ice shelf. If the shelf is tilted toward the continent, the rift is under compression, and we see low levels of seismicity; if the shelf is tilted seaward, the rift is subjected to additional extensional stress, and we see high levels of seismicity. Using the CATS2008 tide model (Padman et al., 2002), we find that this 5-hr delay corresponds to a maximum tidally induced tilt of the entire RIS (Figure 2). We calculate the maximum stretching stress that could affect the rift associated with this tilt to be $\rho_i g \alpha L$ where ρ_i is the ice density, g is the acceleration due to gravity, L is the distance from the rift to the ice front, and α is the tidally induced tilt angle. For $\alpha = 10 * 10^{-7}$, this suggests maximum stretching stresses on the order of 1 kPa, in agreement with stress due to sea surface tilt calculated by Bassis

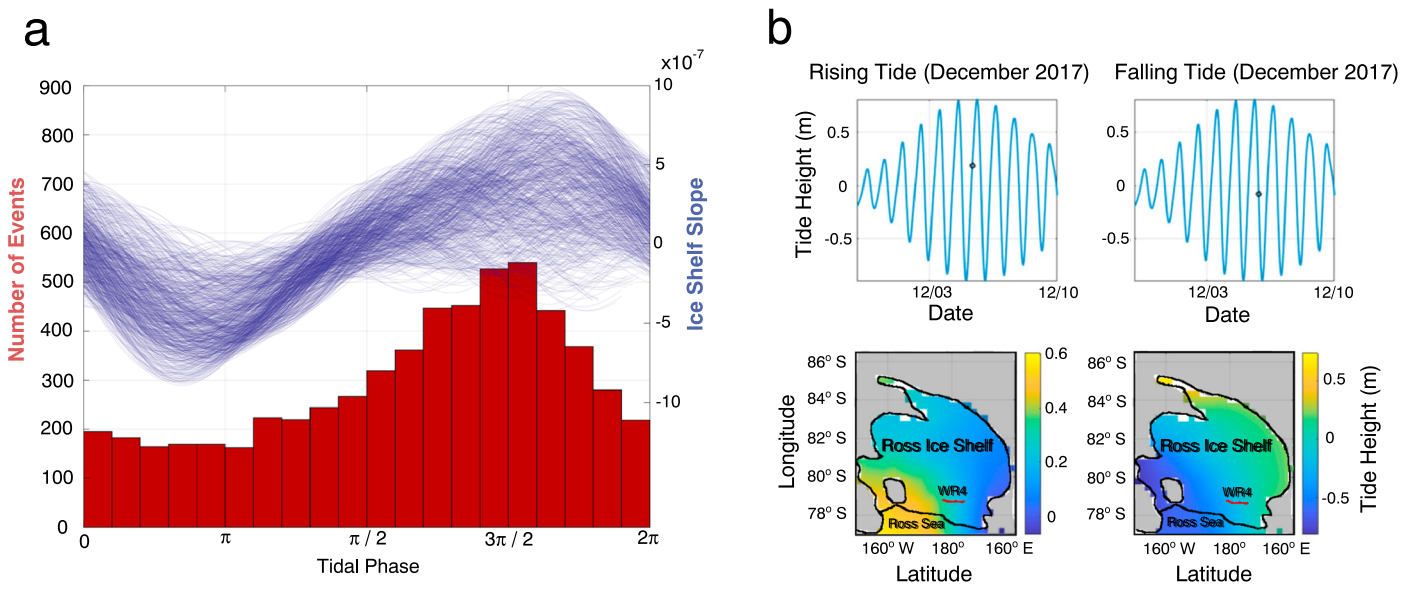

Figure 2. Tidal slope and rift seismicity. (a) Histogram of event timing as a function of tidal phase plotted with ocean surface slope (blue lines) for each tidal cycle during the duration of the deployment. (b) Modeled tidal heights at 81.75°S, −175°W, the center of the ice shelf (top), and in map view across the Ross Ice Shelf (bottom) demonstrating the ocean surface slope relationships shown in (a). Red dots in the top figures identify the timing of the ice shelf height maps. Tidal heights were obtained using the CATS2008 tidal model (Padman et al., 2002).

et al. (2008). Our findings are consistent with previous observations of tidally modulated glacial seismicity (Barruol et al., 2013; Podolskiy et al., 2016) and tidally modulated ice shelf flow (Brunt et al., 2010; Makinson et al., 2012). Furthermore, they suggest that stretching stresses from tidal cycles are preferentially released at rifts and may be associated with the processes that widen rifts after formation.

6. Temperature Controls Multiday and Seasonal Patterns in Seismicity

The detected icequakes exhibit a distinct seasonality that correlates with surface temperature data (Figure 3a). Temperature data were recorded by station Gill (Figure 1) of the Antarctic Weather Stations project (Lazzara et al., 2012), at a distance of 80 km from the center of the array. In the Antarctic summer (December/January/February), very low levels of seismicity are observed. However, as soon as temperatures begin to decline rapidly at the beginning of winter in both 2015 and 2016, the average number of events per day increases dramatically, with days containing over 20 events becoming common. Furthermore, large and rapid decreases in temperature appear to be associated with days of particularly high activity. The coldest periods of 2015 and 2016 both correspond to days with the largest number of icequakes. Although seismic noise levels are highest in the summer, examination of the temporal pattern of the larger events shows that the seasonal pattern of seismicity is not due to the seasonality of the seismic noise floor (supporting information S1 and Figure S3).

There are two potential mechanisms that could account for the correlation between icequake activity and temperature. First, ice experiences low temperature embrittlement when loaded in compression (Petrovic, 2003). It is therefore plausible that tidal stresses result in ductile deformation at high temperatures but result in brittle icequake-related deformation at lower temperatures. This explanation is consistent with studies that find seasonal variability of ice shelf material properties (Bromirski & Stephen, 2012).

Second, the uppermost portion of the ice experiences thermal contraction in response to rapid temperature drops and would thus be under tensional stress, as is observed for sea ice during cold weather (Dempsey et al., 2018; Evans & Untersteiner, 1971; Richter-Menge & Elder, 1998). Similar behavior has been observed in some alpine glaciers, which exhibit thermal fracturing in response to cold nighttime temperatures (Podolskiy et al., 2018; Zhang et al., 2019). Although we have not obtained source parameters for these events, the association between the icequakes and tensional tidal stress, and their location in a rift zone, suggests that the events are dominantly tensional. Since both the tidal and the thermal mechanisms produce

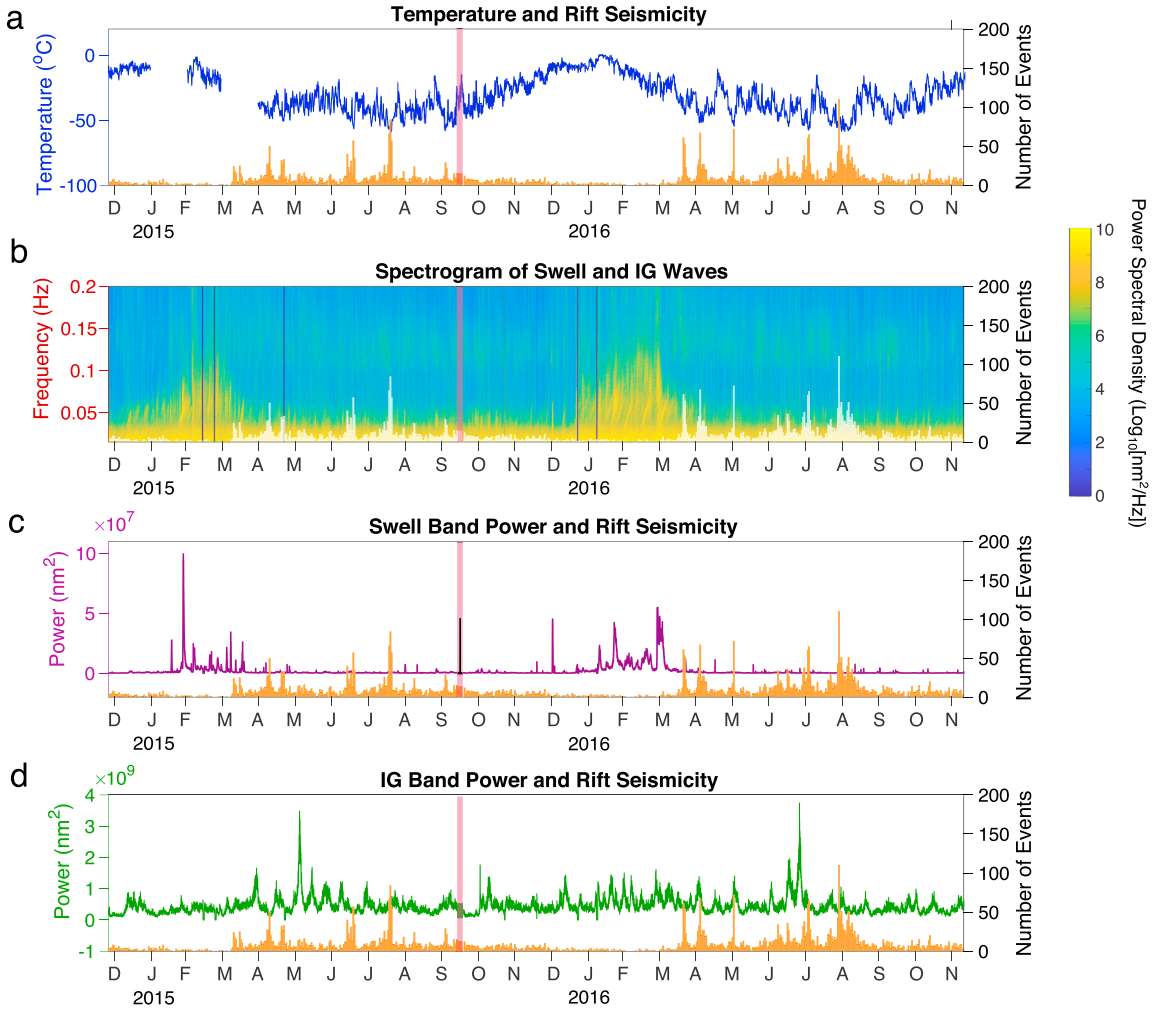

Figure 3. Ocean swell, infragravity (IG) waves, temperature, and rift seismicity. (a) Surface temperatures from Automatic Weather Station Gill (blue), plotted with the histogram of rift seismicity (orange) as a function of time during the deployment. (b) Spectrogram showing swell and IG wave band power. Black bars indicate data gaps. (c) Ocean swell power (purple line) in the frequency band 0.03–0.15 Hz plotted with the histogram of rift seismicity. (d) IG wave power (green line) in the frequency band 0.015–0.03 Hz, plotted with the histogram of rift seismicity. Spectral analysis used long period north-south component data from station DR10. The Illapel, Chile tsunami arrival is indicated in pink on each panel of the figure. The seasonal trend in seismicity corresponds to seasonal temperature variation, and wintertime swarms coincide with periods of extreme cold and not with swell or IG waves.

horizontal tensional stress, it is likely that they act in concert. Because short-period temperature fluctuations only propagate to a depth of several meters in glacial ice (Giese & Hawley, 2015), shallow icequake locations are consistent with the correlation between icequake activity and surface air temperatures. However, we note the possibility that enhanced cold air circulation within the rift may cause thermal contraction deeper in the ice than would otherwise be possible.

7. Rift Seismicity Is Insensitive to Ocean Swell and IG Waves

Both ocean swell and IG waves are poorly correlated with seismicity at WR4. We analyze the contribution of swell and IG waves by spectral analysis of the horizontal north-south component data from station DR10, since ocean waves generate large horizontal displacements on RIS (Bromirski et al., 2017). Because sea ice attenuates ocean waves (Massom et al., 2018), swell energy only reaches the array during the austral summer, when seasonal sea ice is minimal in extent. Rift seismicity is far less frequent in the austral summer than in the winter, and periods that contain significant swell energy correspond to very low levels of seismicity at the rift (Figures 3b and 3c). Furthermore, when peak levels of seismicity are observed during wintertime icequake swarms, minimal power is observed in the swell band.

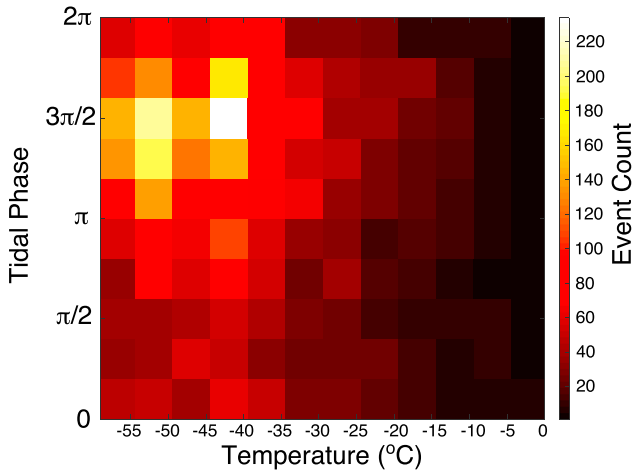

Figure 4. Density plot of number of events as a function of tidal phase and temperature. Temperature data are from weather station Gill (Figure 1). Peak levels of seismicity are observed when temperature is low and when the shelf is most highly sloped downward toward the ice front during falling tide.

IG waves are damped less effectively than swell by winter sea ice (Bromirski & Stephen, 2012), and IG wave excitation of the RIS is detected by the array year-round (Figure 3b). We find that IG band power is poorly correlated with seismicity (Figure 3d). Most swarms occur on days that lack significant IG band power, and the largest IG events recorded at the array do not correspond to swarms of seismicity. Finally, the baseline level of IG power is nearly constant throughout the year and does not explain the seasonality observed in rift seismicity. On 17 September 2015, a tsunami generated by the M_w 8.3 Illapel, Chile earthquake reached the ice shelf, exciting horizontal displacements of about 7 cm at DR10 (Bromirski et al., 2017). The tsunami arrival is marked in Figure 3 and is particularly visible in the swell power time series. However, the tsunami does not correspond to an increase in seismicity at WR4. This is consistent with previous findings that only rifts open to the ocean at the calving front propagate when a tsunami arrives (Walker et al., 2013), further suggesting that WR4 is not subject to significant wave-induced fracture.

8. Conclusions

Two primary environmental factors control rift seismicity at WR4. Diurnally, the timing of events is well-correlated with tidally driven changes in ice shelf slope. Over longer time periods, the timing of events is well-correlated with air temperature, with peak levels of activity in the winter and swarms of events on particularly cold days. The combination of these two factors explains the temporal patterns in seismicity that we observe here and demonstrates the high environmental sensitivity of rift deformation. Figure 4 illustrates that maximal icequake activity occurs during cold periods when the ice shelf is sloping downward toward the ice front. We note that while low levels of icequake activity are observed at low tide, no rift seismicity is observed above −10 °C. From this analysis, we conclude that although thermal and tidal stresses are both important in generating shallow icequake activity, temperature exerts the most significant control on brittle deformation at WR4.

The sequence of WR4 icequakes differs from patterns of seismicity seen in propagating rifts, and the correspondence of the locations to en echelon shear zone features suggests that fracture may occur within the melange filling the rift. Swell and IG waves were not correlated with rift seismicity, though they may still exert some influence on rift behavior at RIS and at other ice shelves. The timing of rift activity at WR4 appears to be primarily modulated by thermal and tidal stresses arising from fluctuations in air temperature and changes in ice shelf slope, and this work represents a novel demonstration of tidal influence on ice shelf processes far from the grounding line. On the RIS, thermal and tidal stresses act in concert with ice shelf stresses, but not wave-induced stresses, to drive brittle deformation that may widen a major rift.

Acknowledgments
NSF grants PLR-1142518, 1141916, and 1142126 supported S. D. Olinger and D. A. Wiens, R. C. Aster, and A. A. Nyblade respectively. NSF grant PLR-1246151 supported P. D. Bromirski, P. Gerstoft, and Z. Chen. NSF grant OPP-1744856 and CAL-DPR-C1670002 also supported P. D. Bromirski. NSF grant PLR-1246416 supported R. A. Stephen. The Incorporated Research Institutions for Seismology (IRIS) and the PASSCAL Instrument Center at New Mexico Tech provided seismic instruments and deployment support. The RIS seismic data (network code XH) are archived at the IRIS Data Management Center (http://ds.iris.edu/ds/nodes/dmc/). S. D. Olinger catalogued and located icequakes, analyzed seismicity and environmental forcing, and drafted the manuscript. D. A. Wiens and B. P. Lipovsky provided significant contributions to the analysis and interpretation of results and to the manuscript text. D. A. Wiens, R. C. Aster, A. A. Nyblade, R. A. Stephen, P. Gerstoft, and P. D. Bromirski collaborated to design and obtain funding for the deployment. D. A. Wiens, R. C. Aster, R. A. Stephen, P. Gerstoft, P. D. Bromirski, and Z. Chen deployed and serviced seismographs in Antarctica. All authors provided valuable feedback, comments, and edits to the manuscript text. Special thanks to Patrick Shore for guidance throughout the research process.

References

Aki, K. (1967). Scaling law of seismic spectrum. *Journal of Geophysical Research*, *72*(4), 1217–1231. Retrieved from https://agupubs.onlinelibrary.wiley.com/doi/abs/10.1029/JZ072i004p01217, https://doi.org/10.1029/JZ072i004p01217

Banwell, A. (2017). Ice-shelf stability questioned. *Nature*, *544*, 306–307. Retrieved from https://doi.org/10.1038/544306a

Barruol, G., Cordier, E., Bascou, J., Fontaine, F. R., Legrésy, B., & Lescarmontier, L. (2013). Tide-induced microseismicity in the Mertz glacier grounding area, East Antarctica. *Geophysical Research Letters*, *40*, 5412–5416. Retrieved from https://doi.org/10.1002/2013GL057814

Bassis, J. N., Coleman, R., Fricker, H. A., & Minster, J. B. (2005). Episodic propagation of a rift on the Amery Ice Shelf, East Antarctica. *Geophysical Research Letters*, *32*, L06502. Retrieved from https://doi.org/10.1029/2004GL022048

Bassis, J. N., Fricker, H. A., Coleman, R., Bock, Y., Behrens, J., Darnell, D., et al. (2007). Seismicity and deformation associated with ice-shelf rift propagation. *Journal of Glaciology*, *53*(183), 523–536. https://doi.org/10.3189/002214307784409207

Bassis, J. N., Fricker, H. A., Coleman, R., & Minster, J.-B. (2008). An investigation into the forces that drive ice-shelf rift propagation on the Amery Ice Shelf, East Antarctica. *Journal of Glaciology*, *54*(184), 17–27. https://doi.org/10.3189/002214308784409116

Benn, D. I., Warren, C. R., & Mottram, R. H. (2007). Calving processes and the dynamics of calving glaciers. *Earth-Science Reviews*, *82*(3), 143–179. Retrieved from http://www.sciencedirect.com/science/article/pii/S0012825207000396, https://doi.org/10.1016/j.earscirev.2007.02.002

Borstad, C., McGrath, D., & Pope, A. (2017). Fracture propagation and stability of ice shelves governed by ice shelf heterogeneity. *Geophysical Research Letters*, *44*, 4186–4194. https://doi.org/10.1002/2017GL072648

Bromirski, P. D., Chen, Z., Stephen, R. A., Gerstoft, P., Arcas, D., Diez, A., et al. (2017). Tsunami and infragravity waves impacting Antarctic ice shelves. *Journal of Geophysical Research: Oceans*, *122*, 5786–5801. Retrieved from https://doi.org/10.1002/2017JC012913

Bromirski, P. D., Diez, A., Gerstoft, P., Stephen, R. A., Bolmer, T., Wiens, D. A., et al. (2015). Ross Ice Shelf vibrations. *Geophysical Research Letters*, *42*, 7589–7597. Retrieved from https://doi.org/10.1002/2015GL065284

Bromirski, P. D., Sergienko, O. V., & MacAyeal, D. R. (2010). Transoceanic infragravity waves impacting Antarctic ice shelves. *Geophysical Research Letters*, *37*, L02502. Retrieved from https://doi.org/10.1029/2009GL041488

Bromirski, P. D., & Stephen, R. A. (2012). Response of the Ross Ice Shelf, Antarctica, to ocean gravity-wave forcing. *Annals of Glaciology*, *53*(60), 163–172. https://doi.org/10.3189/2012AoG60A058

Brunt, K., King, M., Fricker, H., & Macayeal, D (2010). Flow of the Ross Ice Shelf, Antarctica, is modulated by the ocean tide. *Journal of Glaciology*, *56*, 157–161. https://doi.org/10.3189/002214310791190875

Brunt, K. M., Okal, E. A., & MacAyeal, D. R. (2011). Antarctic ice-shelf calving triggered by the Honshu (Japan) earthquake and tsunami, March 2011. *Journal of Glaciology*, *57*(205), 785–788. https://doi.org/10.3189/002214311798043681

Cathles, L. M., Okal, E. A., & MacAyeal, D. R. (2009). Seismic observations of sea swell on the floating Ross Ice Shelf, Antarctica. *Journal of Geophysical Research*, *114*, F02015. Retrieved from https://doi.org/10.1029/2007JF000934

Dempsey, J. P., Cole, D. M., & Wang, S. (2018). Tensile fracture of a single crack in first-year sea ice. *Philosophical Transactions of the Royal Society A*, *376*(2129), 20170346. Retrieved from https://app.dimensions.ai/details/publication/pub.1106250569 and http://rsta.royalsocietypublishing.org/content/376/2129/20170346.full.pdf (Exported from https://app.dimensions.ai on 2019/03/14) https://doi.org/10.1098/rsta.2017.0346

Evans, R. J., & Untersteiner, N. (1971). Thermal cracks in floating ice sheets. *Journal of Geophysical Research*, *76*(3), 694–703. Retrieved from https://doi.org/10.1029/JC076i003p00694

Fricker, H. A., Young, N. W., Coleman, R., Bassis, J. N., & Minster, J. B. (2005). Multi-year monitoring of rift propagation on the Amery Ice Shelf, East Antarctica. *Geophysical Research Letters*, *32*, L02502. Retrieved from https://doi.org/10.1029/2004GL021036

Giese, A. L., & Hawley, R. L. (2015). Reconstructing thermal properties of firn at Summit, Greenland, from a temperature profile time series. *Journal of Glaciology*, *61*(227), 503–510. Retrieved from https://doi.org/10.3189/2015JoG14J204

Heeszel, D. S., Fricker, H. A., Bassis, J. N., O'Neel, S., & Walter, F. (2014). Seismicity within a propagating ice shelf rift: The relationship between icequake locations and ice shelf structure. *Journal of Geophysical Research: Earth Surface*, *119*, 731–744. Retrieved from https://doi.org/10.1002/2013JF002849

Holdsworth, G., & Glynn, J. (1978). Iceberg calving from floating glaciers by a vibrating mechanism. *Nature*, *274*, 464–466. https://doi.org/10.1038/274464a0

Hulbe, C. L., Klinger, M., Masterson, M., Catania, G., Cruikshank, K., & Bugni, A. (2016). Tidal bending and strand cracks at the Kamb Ice Stream grounding line, West Antarctica. *Journal of Glaciology*, *62*(235), 816–824. https://doi.org/10.1017/jog.2016.74

Hulbe, C. L., LeDoux, C., & Cruikshank, K. (2010a). Propagation of long fractures in the Ronne Ice Shelf, Antarctica, investigated using a numerical model of fracture propagation. *Journal of Glaciology*, *56*(197), 459–472. https://doi.org/10.3189/002214310792447743

Kulessa, B., Jansen, D., Luckman, A. J., King, E. C., & Sammonds, P. R. (2014). Marine ice regulates the future stability of a large Antarctic ice shelf. *Nature Communications*, *5*, 3707.

Larour, E., Rignot, E., & Aubry, D. (2004). Modelling of rift propagation on ronne ice shelf, antarctica, and sensitivity to climate change. *Geophysical Research Letters*, *31*, L16404. Retrieved from https://doi.org/10.1029/2004GL020077

Lazzara, M. A., Weidner, G. A., Keller, L. M., Thom, J. E., & Cassano, J. J. (2012). Antarctic Automatic Weather Station program: 30 years of polar observation. *Bulletin of the American Meteorological Society*, *93*(10), 1519–1537. Retrieved from https://doi.org/10.1175/BAMS-D-11-00015.1

LeDoux, C. M., Hulbe, C. L., Forbes, M. P., Scambos, T. A., & Alley, K. (2017). Structural provinces of the Ross Ice Shelf, Antarctica. *Annals of Glaciology*, *58*(75pt1), 88–98. https://doi.org/10.1017/aog.2017.24

Lipovsky, B (2018). Ice shelf rift propagation and the mechanics of wave-induced fracture. *Journal of Geophysical Research: Oceans*, *123*, 4014–4033. Retrieved from https://doi.org/10.1029/2017JC013664

Lough, A. C., Barcheck, C. G., Wiens, D. A., Nyblade, A., & Anandakrishnan, S. (2015). A previously unreported type of seismic source in the firn layer of the East Antarctic Ice Sheet. *Journal of Geophysical Research: Earth Surface*, *120*, 2237–2252. Retrieved from https://doi.org/10.1002/2015JF003658

MacAyeal, D. R., Okal, E. A., Aster, R. C., & Bassis, J. N. (2008). Seismic and hydroacoustic tremor generated by colliding icebergs. *Journal of Geophysical Research*, *113*, F03011. Retrieved from https://doi.org/10.1029/2008JF001005

MacAyeal, D. R., Rignot, E., & Hulbe, C. L. (1998). Ice-shelf dynamics near the front of the Filchner-Ronne Ice Shelf, Antarctica, revealed by SAR interferometry: Model/interferogram comparison. *Journal of Glaciology*, *44*(147), 419–428. https://doi.org/10.3189/S0022143000002744

Makinson, K., King, M. A., Nicholls, K. W., & Gudmundsson, G. H. (2012). Diurnal and semidiurnal tide-induced lateral movement of Ronne Ice Shelf, Antarctica. *Geophysical Research Letters*, *39*, L10501. Retrieved from https://doi.org/10.1029/2012GL051636

Massom, R. A., Scambos, T. A., Bennetts, L. G., Reid, P., Squire, V. A., & Stammerjohn, S. E. (2018). Antarctic ice shelf disintegration triggered by sea ice loss and ocean swell. *Nature*, *558*(7710), 383–389. Retrieved from https://doi.org/10.1038/s41586-018-0212-1

McGrath, D., Steffen, K., Holland, P. R., Scambos, T., Rajaram, H., Abdalati, W., & Rignot, E. (2014). The structure and effect of suture zones in the Larsen C Ice Shelf, Antarctica. *Journal of Geophysical Research: Earth Surface*, *119*, 588–602. https://doi.org/10.1029/2019GL082842

Padman, L., Fricker, H. A., Coleman, R., Howard, S., & Erofeeva, L. (2002). A new tide model for the Antarctic ice shelves and seas. *Annals of Glaciology*, *34*, 247–254. https://doi.org/10.3189/172756402781817752

Petrovic, J. (2003). Review mechanical properties of ice and snow. *Journal of Materials Science*, *38*, 1–6. https://doi.org/10.1023/A:1021134128038

Podolskiy, E. A., Fujita, K., Sunako, S., Tsushima, A., & Kayastha, R. B. (2018). Nocturnal thermal fracturing of a Himalayan debris-covered glacier revealed by ambient seismic noise. *Geophysical Research Letters*, *45*, 9699–9709. Retrieved from https://doi.org/10.1029/2018GL079653

Podolskiy, E. A., Sugiyama, S., Funk, M., Walter, F., Genco, R., Tsutaki, S., et al. (2016). Tide-modulated ice flow variations drive seismicity near the calving front of Bowdoin Glacier, Greenland. *Geophysical Research Letters*, *43*, 2036–2044. Retrieved from https://doi.org/10.1002/2016GL067743

Press, F., & Ewing, M. (1951). Propagation of elastic waves in a floating ice sheet. *Eos, Transactions American Geophysical Union*, *32*(5), 673–678. Retrieved from https://doi.org/10.1029/TR032i005p00673

Richter-Menge, J. A., & Elder, B. C. (1998). Characteristics of pack ice stress in the Alaskan Beaufort Sea. *Journal of Geophysical Research*, *103*(C10), 21,817–21,829. Retrieved from https://doi.org/10.1029/98JC01261

Rignot, E., & MacAyeal, D. R. (1998). Ice-shelf dynamics near the front of the Filchner–Ronne Ice Shelf, Antarctica, revealed by SAR interferometry. *Journal of Glaciology*, *44*(147), 405–418. https://doi.org/10.3189/S0022143000002732

Toffoli, A., & Bitner-Gregersen, E. M. (2017). Types of ocean surface waves, wave classification. In J. Carlton, P. Jukes, & Y. S. Choo (Eds.), *Encyclopedia of Maritime and Offshore Engineering*. Retrieved from https://doi.org/10.1002/9781118476406.emoe077

Walker, C., Bassis, J., Fricker, H., & Czerwinski, R. (2013). Structural and environmental controls on Antarctic ice shelf rift propagation inferred from satellite monitoring. *Journal of Geophysical Research: Earth Surface*, *118*, 2354–2364. Retrieved from https://doi.org/10.1002/2013JF002742

Zhang, T., Chen, Y., Ding, M., Shen, Z., Yang, Y., & Guan, Q. (2019). Air-temperature control on diurnal variations in microseismicity at Laohugou Glacier no. 12, Qilian Mountains. *Annals of Glaciology*, 1–12. https://doi.org/10.1017/aog.2018.34